

# RHINO: Regularizing the Hash-based Implicit Neural Representation

Hao Zhu\* · Fengyi Liu\* · Qi Zhang · Xun Cao · Zhan Ma

Received: date / Accepted: date

**Abstract** The use of Implicit Neural Representation (INR) through a hash-table has demonstrated impressive effectiveness and efficiency in characterizing intricate signals. However, current state-of-the-art methods exhibit insufficient regularization, often yielding unreliable and noisy results during interpolations. We find that this issue stems from broken gradient flow between input coordinates and indexed hash-keys, where the chain rule attempts to model discrete hash-keys, rather than the continuous coordinates. To tackle this concern, we introduce RHINO, in which a continuous analytical function is incorporated to facilitate regularization by connecting the input coordinate and the network additionally without modifying the architecture of current hash-based INRs. This connection ensures a seamless backpropagation of gradients from the network’s output back to the input coordinates, thereby enhancing regularization. Our experimental results not only showcase the broadened regularization capability across different hash-based INRs like DINER and Instant NGP, but also across a variety of tasks such as image fitting, representation of signed distance functions, and optimization of 5D static / 6D dynamic neural radiance fields. Notably, RHINO outperforms current state-of-the-art techniques in both quality and speed, affirming its superiority.

---

The first two authors contributed equally. The work was supported by National Key Research and Development Project of China (2022YFF0902402) and NSFC (T2221003, 62101242, 62022038, 62025108).

---

Hao Zhu, Fengyi Liu, Xun Cao, Zhan Ma  
 School of Electronic Science and Engineering, Nanjing University, Nanjing, 210023, China  
 E-mail: caoxun@nju.edu.cn, mazhan@nju.edu.cn

Qi Zhang  
 Tencent AI Lab, Shenzhen, 518054, China

**Keywords** Implicit Neural Representation, Regularization, Static/Dynamic Neural Radiance Field, Signed Distance Function

## 1 Introduction

Implicit neural representation (INR) ([Sitzmann et al., 2020](#)), which characterizes a signal by establishing a continuous mapping function between the coordinate and the attribute using a neural network, is drawing intensive attention. Due to its versatile capability of seamlessly incorporating differentiable physical mechanisms, INR holds significant potential for tackling a range of domain-specific inverse problems, particularly in situations where large scale paired datasets are unavailable, ranging from the cross-model media representation/compression ([Gao et al., 2022; Strümpler et al., 2022](#)) in image processing to reconstruction/rendering ([Mildenhall et al., 2020; Tewari et al., 2022; Zhu et al., 2023b](#)) in vision/graphics, from hologram/tomography imaging ([Zhu et al., 2022; Liu et al., 2022](#)) in microscopy to meta-surface design ([Chen et al., 2020](#)) in materials, from partial differential equations solver ([Raissi et al., 2019; Karniadakis et al., 2021](#)) in computational math to fluid simulation ([Raissi et al., 2020](#)) in hydrodynamics. INR is catalyzing a profound transformation in the landscape of signal processing, heralding a paradigm shift that holds immense promise for diverse applications.

However, the expressive power of current INR techniques is limited. For example, they often suffer from the well-known spectral bias ([Rahaman et al., 2019](#)) that only the information corresponding to the pre-encoded frequencies could be well represented. As a result, it is essential to encode more frequency bases ([Tancik et al., 2020; Sitzmann et al., 2020; Lindell et al., 2022; Ramasinghe and Lucey, 2022; Yüce et al., 2022; Saragadam et al., 2023](#)) into the

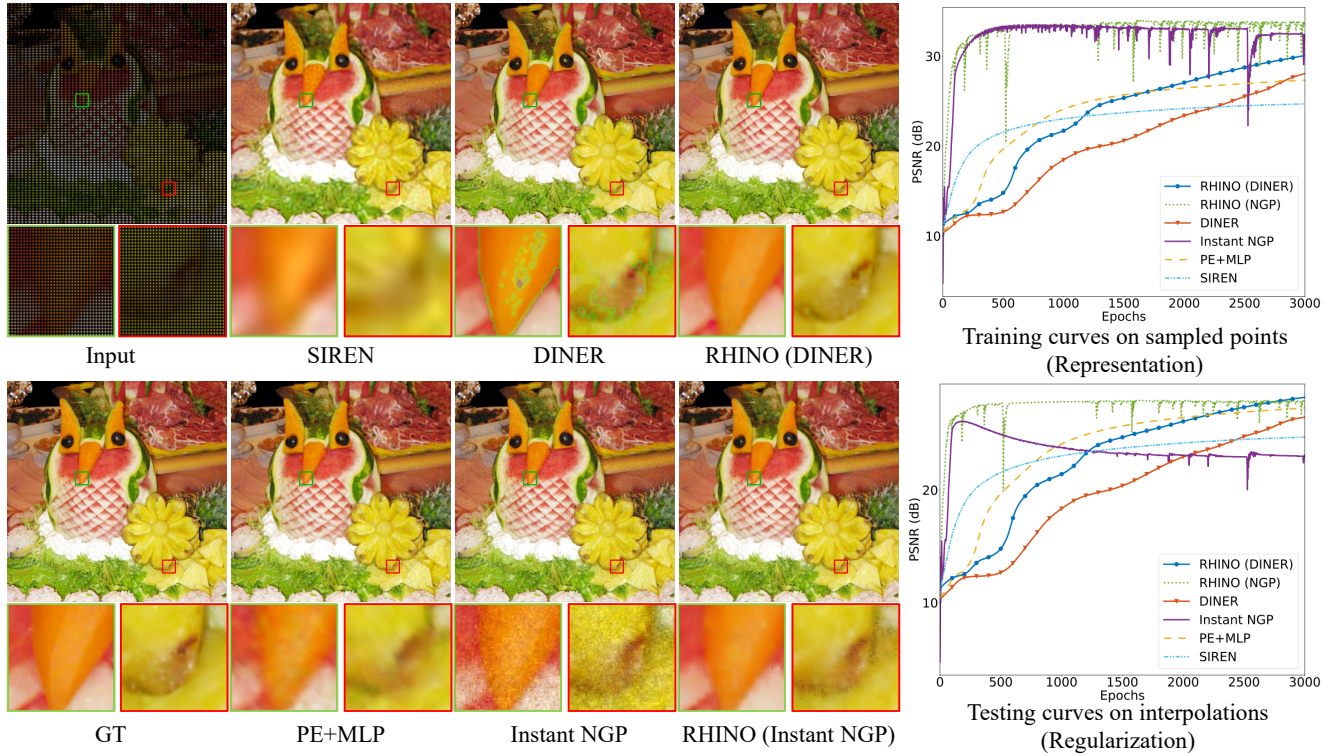


Fig. 1: Comparisons of different INRs for representing and interpolating the 2D image 'Pineapple'. Traditional function-expansion-based INRs (SIREN and PE+MLP) suffer from spectral bias, thus over-smooth textures are produced. Hash-based INRs (DINER and Instant NGP) improve the expressive power, however noisy artifacts appear in the interpolations. RHINO improves both the expressive power and the regularization of hash-based INRs.

neural network at the cost of exceptionally slow convergence. Recently, hash-based methods have garnered significant attention as they circumvent the constraints imposed by spectral bias by replacing the frequency encoding with learnable hash-key indexing (Liu et al., 2020; Takikawa et al., 2021; Chabra et al., 2020; Jiang et al., 2020; Müller et al., 2022; Kang et al., 2022; Xie et al., 2023). They have achieved notably higher Peak Signal-to-Noise Ratio (PSNR) values, often even reaching around  $\sim 90\text{dB}$  (Zhu et al., 2023a), for tasks involving signal representation. However, the regularization ability has been considerably weakened or even entirely lost, leading to the emergence of noisy artifacts particularly in tasks that necessitate interpolation.

We have identified a crucial factor responsible for the lost regularization seen in hash-based methods. This phenomenon arises due to a disruption in the gradient flow between the output of the neural network and the input coordinate. The root cause of this issue lies in the indexing of the hash-key, which is based on the relative order of the input coordinate among all coordinates instead of transforming the coordinate using continuous and analytical functions. Consequently, the chain rule, a fundamental principle in calculus, is broken between the input coordinate and the indexed hash-key. This breakage has significant ramifications. The

optimization processes for both the hash-keys and the network parameters become detached from the input coordinate. Consequently, the interpolations on coordinates that do not appear in the training process exhibit unwanted artifacts. In light of these challenges, we present an innovative solution named RHINO. This novel approach involves the establishment of an additional continuous connection between the input coordinate and the subsequent network.

RHINO stands as a universal regularization framework designed for a diverse range of hash-based INR backbones. The supplementary connection it introduces holds the potential to substantially bolster regularization performance while concurrently enhancing the system's representation capabilities. Furthermore, the incremental computational overhead incurred remains notably minimal. As shown in Fig. 1, the regularization and representation aspects of two contemporary state-of-the-art methodologies, specifically Instant NGP (Müller et al., 2022) and DINER (Xie et al., 2023), both showcase improvements compared to their original incarnations. Moving forward, to verify the performance of the RHINO on inverse problems, extensive experiments spanning various tasks are conducted, including the 3D signed distance function representation, 5D static, and 6D dynamic neural radiance fields reconstruction. Quantitative and qual-

itative comparisons with state-of-the-art methods demonstrate the effectiveness and efficiency of the RHINO. Specifically, the main contributions of the work include,

1. We observe and analyse the phenomenon that current hash-based INRs suffer a notable lack of regularization, resulting in noisy artifacts on interpolated points.
2. We propose a universal regularization framework for hash-based INRs, which serves to enhance both regularization and representation performance while incurring only a minor increase in computational time.
3. We substantiate that RHINO surpasses prior function-expansion-based and hash-based INRs in the domains of 2D image fitting, and 3D shape representation, as well as 5D static and 6D dynamic neural rendering.

## 2 Related work

This section gives a brief review of existing methods for implicit neural representations. RHINO draws inspiration from hash-based representations and the regularization of INR, we outline some of the related works here to set the context.

### 2.1 Neural Scene Representation and Rendering.

The use of neural network to represent the geometry and appearance of a scene has witnessed a significant upsurge in popularity. Traditional methods explicitly represent scenes using point clouds (Pumarola et al., 2020; Wu et al., 2020; Rückert et al., 2022), meshes (Wang et al., 2018; Thies et al., 2019; Huang et al., 2020), or voxels (Wang et al., 2017; Lombardi et al., 2019; Sitzmann et al., 2019). In contrast, neural network promise 3D-structure-aware and memory-economic scene representations for radiance fields (Mildenhall et al., 2020; Barron et al., 2021; Müller et al., 2022), signal distance fields (SDF) (Chabra et al., 2020; Yariv et al., 2021; Genova et al., 2020), or occupancy networks of objects (Mescheder et al., 2019; Peng et al., 2020; Niemeyer et al., 2019).

A remarkable advancement in this field is neural radiance fields (NeRF), which learns a continuous volumetric representation of a 3D scene from a set of images, enabling the rendering of photo-realistic views through ray tracing. NeRF has recently been investigated for various tasks, such as view synthesis for dynamic scenes (Li et al., 2022; Wang et al., 2022; Fang et al., 2022; Fridovich-Keil et al., 2023; Li et al., 2023b), implicit surface reconstruction (Wang et al., 2021a; Yariv et al., 2021; Yu et al., 2022), generalizable image-based rendering (Wang et al., 2021b; Chen et al., 2021; Johari et al., 2022; Huang et al., 2023b), and scene editing (Martin-Brualla et al., 2021; Yuan et al., 2022; Bao et al., 2023). Recently, 2D generative image models (*i.e.*, Generative Adversarial Networks (GANs) (Goodfellow et al., 2014;

Abdal et al., 2019) and diffusion-based methods (Ho et al., 2020; Nichol and Dhariwal, 2021; Saharia et al., 2022)) have been extended and combined with scene representations to enable 3D-aware generation, such as EG3D (Chan et al., 2022), StyleSDF (Or-El et al., 2022), DreamFusion (Poole et al., 2022), and Magic3D (Lin et al., 2023). Leveraging the benefits of neural scene representations, these approaches have shown remarkable potential in producing realistic and intricate 3D scenes while preserving novel view consistency.

### 2.2 Implicit Neural Representations

Implicit neural representations (INRs), the core component for neural scene representations, are designed to learn continuous functions based on a multi-layer perceptron (MLP) that maps coordinates to visual signals, such as images (Dupont et al., 2021; Sitzmann et al., 2020; Tancik et al., 2020; Lindell et al., 2021), videos (Kasten et al., 2021), and 3D scenes (Martin-Brualla et al., 2021; Wang et al., 2021a). With the widespread application in novel view synthesis (Mildenhall et al., 2020), INRs have rapidly expanded into various fields of vision and signal processing, such as cross-model media representation/compression (Gao et al., 2022; Strümpler et al., 2022), neural camera representations (Huang et al., 2022, 2023a), microscopy imaging (Zhu et al., 2022; Liu et al., 2022) and partial differential equations solver (Raissi et al., 2019; Karniadakis et al., 2021).

In summary, Existing INRs can be roughly classified into two groups: a) function-expansion-based INRs, and b) hash-based INRs. Specifically, Tancik et al. (2020) propose a coordinate-based INR that uses Fourier features of coordinates as input of an MLP to learn high-frequency information of natural signals. Sitzmann et al. (2020) employ periodic activation function (SIREN) as a replacement for the traditional ReLU activation in INRs, enabling fine details of the scene. Recent works reveal that the success of the Fourier features is achieved by viewing the INR as the problem function-expansion using different bases, as a result, classical bases in higher mathematics such as the wavelet bases (Fathony et al., 2020; Saragadam et al., 2023), polynomial bases (Yang et al., 2022) and Gaussian bases (Ramasinghe and Lucey, 2022) have all been successfully integrated into the architecture design of INR. Despite the growing interest and success of coordinate-based INRs, existing techniques often face limitations in their expressive power. Issues such as spectral bias and the need for additional frequency bases for complex scenes continue to pose challenges (Yüce et al., 2022).

To overcome the limitations posed by the spectral bias and to amplify the expressive capabilities of INRs, recent techniques (Liu et al., 2020; Takikawa et al., 2021; Chabra et al., 2020; Jiang et al., 2020; Müller et al., 2022; Yu et al., 2022; Kang et al., 2022; Xie et al., 2023; Sun et al., 2022;

(Chan et al., 2022; Chen et al., 2022) have introduced hash-based INRs. These innovative approaches replace frequency encoding with learned hash-key indexing, thereby bestowing these models with significantly enhanced scene representation capabilities. In particular, Müller et al. (2022) make use of learned hash functions to map coordinates to compact hash keys, which are then employed to index a set of optimized features for various vision signal reconstruction. Xie et al. (2023) propose disorder-invariant INR by incorporating a hash-table to a traditional INR backbone. This innovative representation ensures that coordinates map into the same distribution, which in turn enables the projected signal to be more accurately modeled by the subsequent INR network. As a result, this method significantly mitigates the issue of spectral bias, leading to improved performance in various signal processing tasks.

By expanding and refining the potential of hash-based INRs through the incorporation of learned hash functions, these methodologies play a pivotal role in propelling the continuous evolution of neural scene representation. Nevertheless, an important consideration arises due to the fact that hash-based INRs employ hash-keys as the network input instead of the raw coordinates (see Sec. 3 for details). This approach could potentially lead to a substantial reduction or even complete loss of their regularization capacity when handling unseen coordinates. The consequence of this diminished regularization is the emergence of disruptive noisy artifacts, particularly in tasks that necessitate interpolation. Hence, it becomes imperative to strike a harmonious balance between the augmented expressive power offered by hash-based INRs and the preservation of robust regularization capabilities.

### 2.3 Regularizing the INR

Apart from expressive power, regularization (*i.e.*, interpolations on points not present in the training set) is another crucial metric that determines the performance of INRs for signals requiring continuous representation, such as neural radiance field optimization for high-quality novel view synthesis at any position (Mildenhall et al., 2020).

Although numerous efforts have been made to regularize classical deep neural networks (Srivastava et al., 2014; Maennel et al., 2018; Heiss et al., 2019; Kubo et al., 2019), there are a few works on regularizing the INR. Ramasinghe et al. (2022) find that a shallow MLP network tends to suppress lower frequencies when the hyper-parameters or depth is increased, resulting in noisy interpolations. They propose the gradient loss built from the second to last layer of the MLP for regularizing the noise. Li et al. (2023a) analyse the poor interpolations of INR on nonuniform sampling following the neural tangent kernel theory (Jacot et al., 2018), they

propose the Dirichlet energy regularization by measuring the similarities between rows/columns for a 2D image.

However, all existing works concentrate on regularization for INRs with continuous and analytical gradient flow between the input coordinate and network output. As analyzed in Sec. 3, the continuous function modeled in hash-based INRs is built upon hash-keys rather than input coordinates, breaking the gradient flow between the input coordinate and hash-key and resulting in noisy interpolations in hash-based methods. Consequently, previous regularization methods cannot be directly applied to hash-based INRs.

## 3 Behaviors of the Hash-based INRs

### 3.1 Principle of the Hash-based INRs

Given a paired signal  $Y = \{(\vec{x}_i, \vec{y}_i)\}_{i=1}^N$  with length  $N$ , where  $\vec{x}_i$  and  $\vec{y}_i$  are the  $i$ -th  $d_{in}$ -dimensional coordinate and the corresponding  $d_{out}$ -dimensional attribute. For the convenience of derivation,  $d_{in}$  is set as 1, thus the term  $\vec{x}_i$  is written as  $x_i$  in the following sections. INR characterizes the paired signal by modeling a function mapping between the input coordinate  $x_i$  and the output attribute  $\vec{y}_i$  using an MLP, that is

$$\begin{aligned} \mathbf{z}^0 &= \gamma(x_i), \\ \mathbf{z}^j &= \rho^j (\mathbf{W}^j \mathbf{z}^{j-1} + \mathbf{b}^j), \quad j = 1, \dots, J-1, \\ f_\theta(x) &= \mathbf{W}^J \mathbf{z}^{J-1} + \mathbf{b}^J \end{aligned} \quad (1)$$

where  $\gamma(\cdot)$  refers to the continuous preprocess encoding function such as the commonly used Fourier encoding (Tancik et al., 2020),  $\mathbf{z}^j$  refers to the output of the  $j$ -th layer of the network,  $\theta = \{\mathbf{W}^j, \mathbf{b}^j\}_{j=0}^J$  are the network parameters, where the  $\mathbf{W}^j, \mathbf{b}^j$  are the weight and bias of the  $j$ -th network layer.

However, there is a spectral bias in the function modeled using the Eqn. 1 that the  $f_\theta(x)$  is composed of a linear combination of certain harmonics of the  $\gamma(\cdot)$  (Yüce et al., 2022), *i.e.*,

$$\begin{aligned} f_\theta(x) &\in \left\{ \sum_{\omega' \in \mathcal{F}_\omega} c_{\omega'} \sin(\langle \omega', x \rangle + \phi_{\omega'}) \right\} \\ c_{\omega'}, \phi_{\omega'} &\in \mathbb{Q}, \end{aligned} \quad (2)$$

where  $\mathcal{F}_{\omega'}$  is the frequency set determined by the encoded frequencies in  $\gamma(\cdot)$ ,  $\mathbb{Q}$  is the set of rational number.

To overcome this limitation, the hash-table  $\mathcal{H}$  (Müller et al., 2022; Kang et al., 2022; Xie et al., 2023) is introduced to replace the role of the continuous preprocess function  $\gamma(\cdot)$ , that

$$\mathbf{z}^0 = \mathcal{H}(x_i), \quad (3)$$

where the keys in the hash-table  $\mathcal{H}$  are also updated during the network training following the chain rule. Note that, because

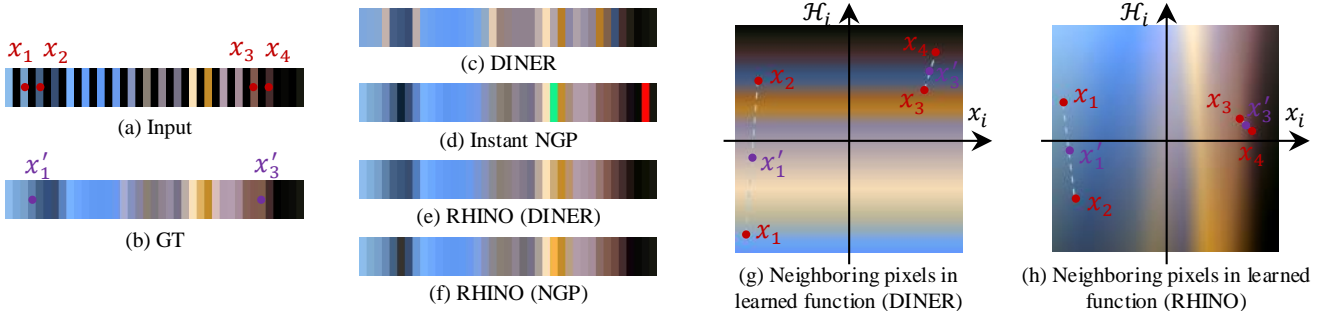


Fig. 2: Comparisons of the hash-based INRs and the proposed RHINO. (a) is the input where the black bands refer to the points to be interpolated. (b) the ground truth. (c) and (d) are interpolations by applying the hash-based INRs, i.e., the DINER (Xie et al., 2023) and the Instant NGP (Müller et al., 2022) directly. (e) and (f) are the results of that using the proposed regularization. (g) and (h) visualize the neighboring pixels and interpolations in the actually learned function of DINER and the RHINO with the DINER backbone, respectively.

the hash-key is indexed according to the relative position of the  $x$  instead of transforming  $x$  with continuous functions, the chain rule is broken between the input coordinate  $x$  and the hash-key, as a result,  $\mathcal{H}(x_i)$  could be directly written as  $\mathcal{H}_i$ . Since the hash-key is also updated in the training process, the optimization of the hash-table in INR could be viewed as finding the solution  $\mathcal{H}_i$  of the function  $f_\theta(\mathcal{H}_i) = \vec{y}_i$  instead of fitting a function  $\theta$  with known input  $\mathcal{H}_i$  and output  $\vec{y}_i$ . As a result, the hash-based INRs (Müller et al., 2022; Xie et al., 2023) have much stronger expressive power than traditional function-expansion-based INRs (Tancik et al., 2020; Sitzmann et al., 2020).

### 3.2 Hash-table Turns off the Regularization

When applying these two types of INRs (i.e., function-expansion-based and hash-based) to the inverse problems with forward physical process  $\mathcal{P}$ , the optimizations of them are,

$$\theta^* = \arg \min_{\theta} \mathcal{L} \left( \mathcal{P} \left( \{f_\theta(x_i)\}_1^N \right), \mathcal{P} \left( \{\vec{y}_i\}_1^N \right) \right) \quad (4a)$$

$$\theta^*, \mathcal{H}^* = \arg \min_{\theta, \mathcal{H}} \mathcal{L} \left( \mathcal{P} \left( \{f_\theta(\mathcal{H}_i)\}_1^N \right), \mathcal{P} \left( \{\vec{y}_i\}_1^N \right) \right), \quad (4b)$$

where  $\mathcal{H}_i$  is the corresponding hash-key of the  $i$ -th coordinate  $x_i$ . It is noticed that the length of  $\mathcal{H}$  is not always equal to the length  $N$  of the signal  $Y$ , actually it could either be larger or smaller than  $N$  according to different strategies of hash indexing, e.g.,  $|\mathcal{H}| = N$  when the full-resolution hash-table is used (Xie et al., 2023),  $|\mathcal{H}| < N$  when multi-scale hash-tables are used for representing gigapixel images (Müller et al., 2022). Mostly,  $\mathcal{H}_i$  is represented by a linear weighting summation (Xie et al., 2023; Kang et al., 2022; Abou-Chakra et al., 2022) or concatenation (Müller et al., 2022) of the

elements  $h_j$  in  $\mathcal{H}$ , i.e.,

$$\mathcal{H}_i \in \left\{ \sum_{j=1}^{|\mathcal{H}|} a_{ij} h_j \right\} \cup \left\{ \bigoplus_{j=1}^{|\mathcal{H}|} a_{ij} h_j \right\} \quad (5)$$

$h_j \in \mathcal{H}, a_{ij} \in \mathbf{Q}^+ \cup \{0\}$

where  $\mathbf{Q}^+$  is the set of positive rational number.

The traditional INR (Eqn. 4a) directly learns the continuous function between the  $x_i$  and the  $\vec{y}_i$ , which means that the interpolation on unsampled points (e.g.,  $x_j, j \notin \{1, 2, \dots, N\}$ ) also follows the regularization of the spectral bias (Yüce et al., 2022). On the other hand, because the gradients flow between the  $x_i$  and the  $\vec{y}_i$  is broken, the hash-based INR (Eqn. 4b) actually learns the continuous function between the  $\mathcal{H}_i^*$  and the  $\vec{y}_i$ . Following the spectral bias (Yüce et al., 2022), there is a regularization on the hash-key  $H_j^*$  that does not appear in the training process. Unfortunately, because the mapping function between the coordinate  $x_i$  and the hash-key  $\mathcal{H}_i^*$  is discontinuous and not analytical, the interpolation on unsampled point  $x_j$  is also discontinuous and not analytical, resulting in the lost regularization.

Fig. 2 demonstrates the above observation. Given a 1D signal with  $d_{in} = 1$  and  $d_{out} = 3$ , hash-based INRs (DINER (Xie et al., 2023) and Instant NGP (Müller et al., 2022)) provide high accuracy for representing the coordinates appeared in the training set (Fig. 2(c) and (d)). However, both of them produce unreliable results for interpolated coordinates (i.e., the black points in Fig. 2(a)). Fig. 2(g) visualizes the learned function  $f_\theta(\mathcal{H}_i)$  of the neural network in DINER. It is noticed that the neighboring pixels (e.g.,  $x_1$  and  $x_2$ , or  $x_3$  and  $x_4$ ) become far from each other, and the line between them will pass through several color bands, thus unreliable interpolations (Fig. 2(c) and (d)) are produced. In summary: **Proposition 1** *The introduction of the hash-table significantly enhances the expressive power of the INRs at the cost of the lost regularization for interpolations.*

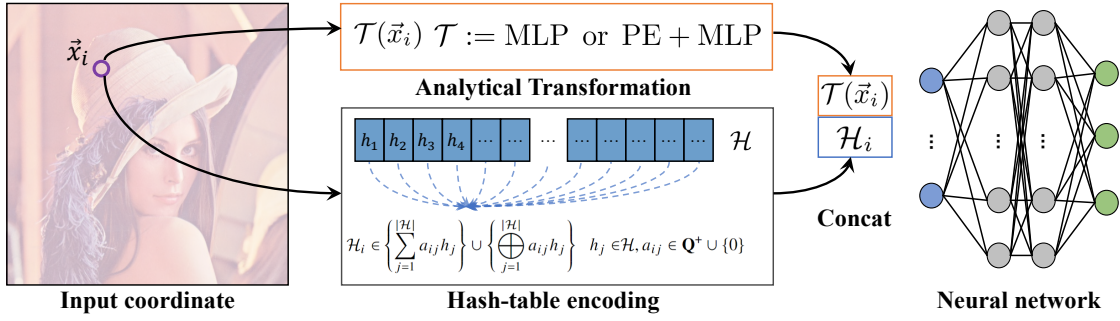


Fig. 3: The architecture of the proposed RHINO. The regularization of previous hash-based INR could all be improved by introducing the input coordinate with an analytical and continuous transformation additionally.

## 4 Regularizing the Hash-based INR

### 4.1 Rebuilding the connections

Because the lost regularization is caused by the broken gradients flow between the  $x_i$  and the  $\vec{y}_i$ , it is useless to compensate the regularization by introducing the traditional smoothness terms (*e.g.*, the total variation (Rudin et al., 1992) and the low rank (Hu et al., 2021) priors) in the loss function. In the hash-based INR, the key for compensating the lost regularization is adding the input coordinate  $x$  with an analytical and continuous transformation  $\mathcal{T}$  to the network, *i.e.*,

$$\theta^*, \mathcal{H}^* = \arg \min_{\theta, \mathcal{H}} \mathcal{L} \left( \mathcal{P} \left( \{f_\theta(\mathcal{H}_i, \mathcal{T}(x_i))\}_1^N \right), \mathcal{P} \left( \{\vec{y}_i\}_1^N \right) \right). \quad (6)$$

Following this idea, we propose the RHINO as shown in Fig. 3, where the architecture of previous hash-based INRs is little altered with an additional input  $\mathcal{T}(x_i)$ . Note that, because the proposed regularization is a universal framework for various encoding (*e.g.*, single scale full-resolution hash-table encoding (Xie et al., 2023) and multi-scale hash-table encoding (Müller et al., 2022)) methods using the hash-table, the middle-bottom panel in Fig. 3 only provides the sketch for constructing hash-keys  $\mathcal{H}_i$ . There are several candidates for the selection of the transformation  $\mathcal{T}$ , such as the identical transformation, a standard MLP network or an MLP with positional encoding. As we will show in the next subsection, these candidates could all improve the regularization of previous pure hash-based methods, but with different behaviors according to the encoded frequencies.

### 4.2 Analysis of Regularization

For better visualizing the structure of the regularization, we focus on the case that the width of the hash-key  $\mathcal{H}_i$  is 1 and the linear weighting summation is used to produce the indexed hash-key. In this case, the learned INR actually builds a continuous function with 2D input, *i.e.*, the  $x_i$  and  $\mathcal{H}_i$ .

Because it is difficult to analyse the properties of the  $f_\theta(\mathcal{H}_i, \mathcal{T}(x_i))$  directly, the 'slicing strategy' is firstly used for analysing different dimensions of the  $f_\theta(\mathcal{H}_i, \mathcal{T}(x_i))$  one by one, then the global property is summarized. In detail, by fixing the  $\mathcal{T}(x_i)$  with different real values, respectively, *e.g.*,  $\mathcal{T}(x_i) = 0, \dots, 1$ , the 2D function  $f_\theta(\mathcal{H}_i, \mathcal{T}(x_i))$  is reduced to a 1D function (*i.e.*,  $f_\theta(\mathcal{H}_i, 0), \dots, f_\theta(\mathcal{H}_i, 1)$ ). The property of each 1D function is equivalent to the previous pure hash-based methods that, 1) the connection between the coordinate and network output is also broken and 2) the distribution of each 1D function also follows the spectral bias. In other words, the regularization is still lost in each 1D function.

However, things change when the attention is focused on another input dimension  $\mathcal{T}(x_i)$  by fixing the  $\mathcal{H}_i$  with real values, *i.e.*,  $f_\theta(0, \mathcal{T}(x_i)), \dots, f_\theta(1, \mathcal{T}(x_i))$ . Because there is an analytical connection between the input coordinate  $x_i$  and network output, these 1D functions are all continuous functions regarding the  $x_i$  and the distribution of each 1D function here follows the spectral bias. In other words, the interpolation on unsampled point  $x_j$  also follows the spectral bias.

Fig. 2 visualizes the above process and the comparisons. Compared with previous pure hash-based INRs (Fig. 2(c) and (d)), the proposed regularization significantly improves their performance on interpolated points (Fig. 2(e) and (f)). Fig. 2(g) and (h) visualize the learned functions without and with regularization. Compared with the one without regularization where the line segment between neighboring pixels will pass through several color bands, the neighboring pixels in the one with regularization are stayed in a similar neighboring color band where the intensity change is more smooth, thus more reliable interpolations (Fig. 2(e) and (f)) are produced. Note that, the regularization performance of the RHINO is not limited to the hash-key  $\mathcal{H}_i$  with width 1, it also works for the case that the width is larger than 1. Fig. 4 shows the learned function with the width 2, it could be noticed that the lost regularization along the  $x_i$ -axis is compensated by adding an analytical function  $\mathcal{T}$ , resulting the

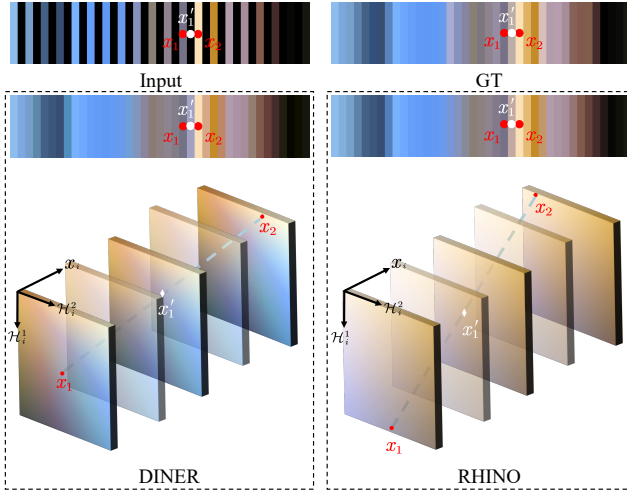


Fig. 4: Comparison of the learned functions with and without  $\mathcal{T}$  for the hash-key  $\mathcal{H}_i$  with width 2. RHINO corrects the wrong purple interpolation  $x'_1$  with the right khaki color.

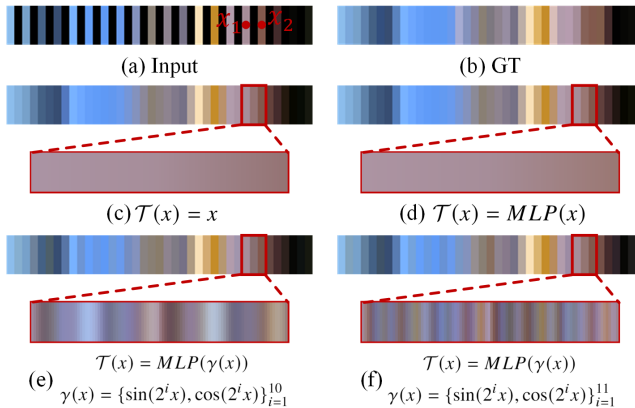


Fig. 5: Comparisons of the proposed regularization with different analytical function  $\mathcal{T}$ . Different analytical functions  $\mathcal{T}$  have similar behavior when only one point is interpolated, however the interpolated textures on dense samples also follow the spectral bias (*i.e.*, the Eqn. 2).

fact that the wrong purple point  $x'_1$  in the DINER is corrected as a khaki point in the RHINO.

**Analytical Transformation  $\mathcal{T}$ .** Different analytical transformation function  $\mathcal{T}$  have different regularization behaviors. Fig. 5 compares the interpolations with different analytical functions, *i.e.*, the identical function  $\mathcal{T}(x) = x$ , a standard MLP without encoding, and Fourier-encoded MLPs (Tancik et al., 2020) with different encoding frequencies. It is noticed that all 4 results produce reliable interpolations when only one point is queried between neighboring points, however the texture distribution changes when denser points are queried. To elaborate, low-frequency textures are generated when employing the identical function as well as the standard MLP without encoding. Conversely, higher-frequency

interpolations emerge when the high-frequency components are encoded within the preprocessing function  $\gamma(\cdot)$  of  $\mathcal{T}(\cdot)$ . In summary:

**Proposition 2** *The additional connection established between the input coordinates and the network enhances the regularization of hash-based INR, where the regularization behavior are influenced by the encoded frequencies within the added analytical function associated with the input coordinates.*

## 5 Experiment

To better demonstrate the performance of the proposed regularization under different inverse problems (*i.e.*, representation, regularization and different dimensions), RHINO is applied in four separate tasks including the 2D image representation, 3D signed distance function representation, 5D static and 6D dynamic neural radiance field reconstruction. Note that, the analytical function  $\mathcal{T}(x)$  is set as the standard MLP with one hidden layer ( $1 \times 64$  neurons), same output dimensions (as the input coordinate) and position encoding ( $\gamma(x) = \{\sin(2^i \pi x), \cos(2^i \pi x)\}_{i=0}^9$ ) in all following experiments.

### 5.1 Image Representation

We use an image representation task to verify the performance of the proposed RHINO and to demonstrate its regularization behavior explicitly. In the experiment, the total 100 high-resolution ( $1200 \times 1200$ ) images from the SAMPLING category of the TESTIMAGES dataset (Asuni and Giachetti, 2014) are used for evaluation. In the experiment, 1/4 pixels are uniformly sampled for training different INRs, then all pixels are used for evaluated the regularization behavior. A total of four baselines are compared, including two classical function-expansion-based methods, PE+MLP (Tancik et al., 2020) and SIREN (Sitzmann et al., 2020), as well as two SOTA hash-based methods, Instant NGP (Müller et al., 2022) and DINER (Xie et al., 2023). As the proposed RHINO is a universal framework, the results of RHINO on the DINER and the Instant NGP are both compared. Note that, the Torch-NGP implementation by Tang (2022) is used throughout the experiment since it is easier to be modified compared with the original Tiny-cuda-nn version (Müller, 2021). For a fair comparison, all methods are set with the same network configuration, *i.e.*, 2 hidden layers with 64 neurons per layer, loss function with  $L_2$  distance between the network output and the ground truth, and are trained for 3000 iterations using the Pytorch and the Adam optimizer with a batchsize  $600 \times 600$  on an Nvidia A100 40GB GPU.

Figs. 1 and 6 compare the regularization behaviors of different methods at 3000 epochs qualitatively. Because there is

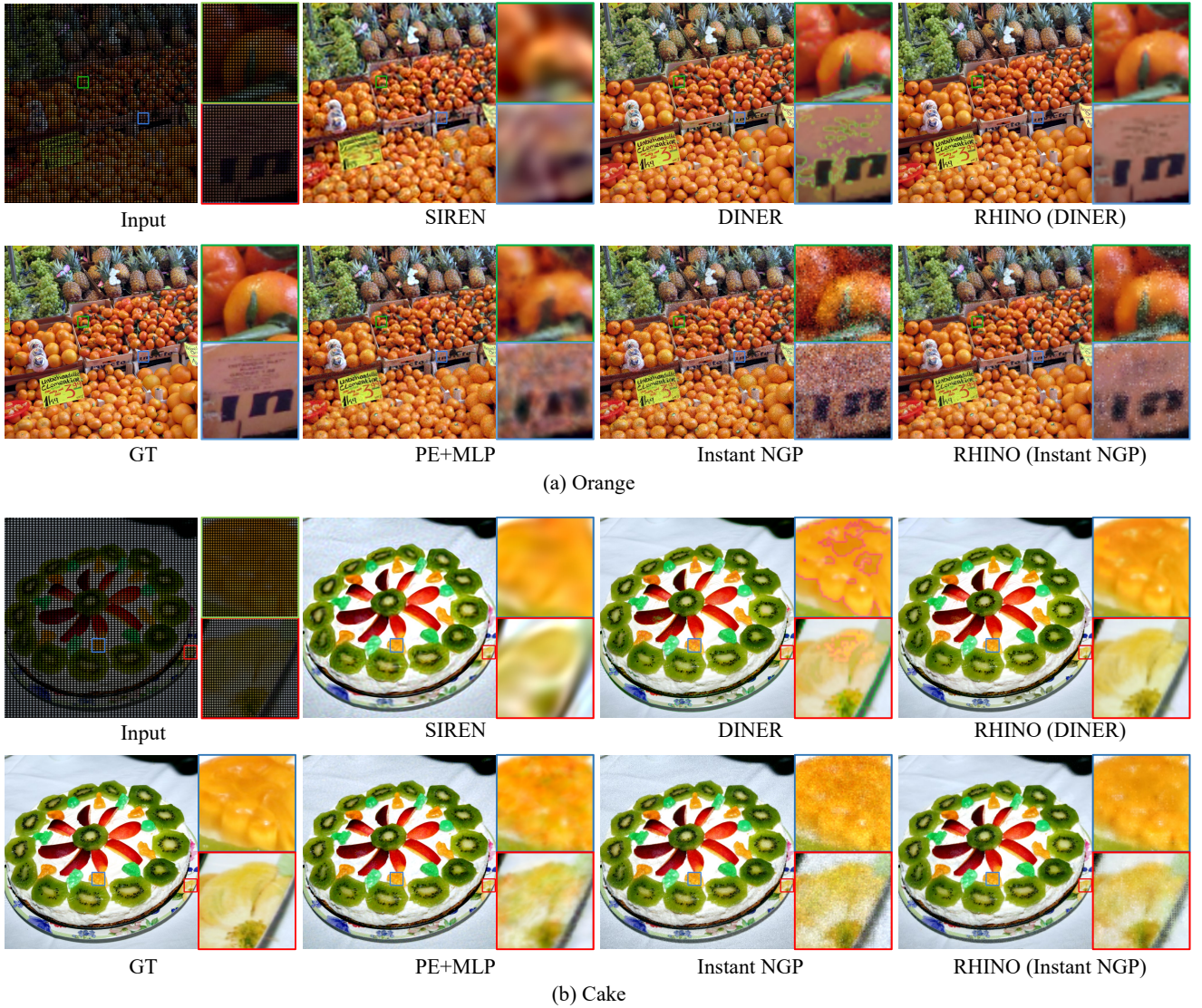


Fig. 6: Comparisons of RHINO with different INR backbones.

Table 1: Comparisons of training time (sec.) for fitting a 2D image with 3000 epochs.

	RHINO (DINER)	RHINO (NGP)	DINER	NGP	PE +MLP	SIREN
Time	15.24	15.37	11.51	9.44	14.50	14.73

an analytical connection between the input coordinate and the output attribute, there are no obvious artifacts in the function-expansion-based INRs (*i.e.*, the SIREN and the PE+MLP). However, as analysed in Sec. 4 that the hash-based INRs focus on optimizing the mapping between the signal attribute and the hash-key instead of the coordinate-self, undesired artifacts appear when the interpolation is applied to the last 3/4 pixels, such as the nose and the pineapple in Fig. 1, the

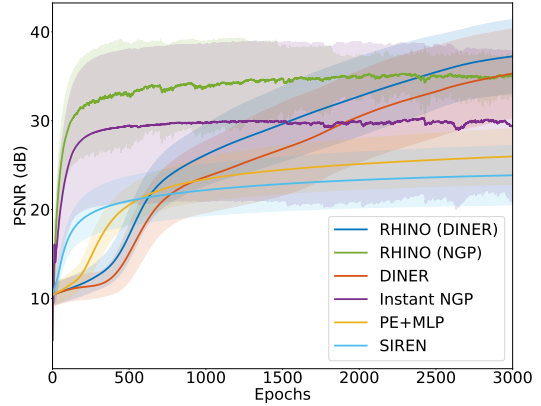


Fig. 7: Training curves of different INRs on fitting 2D image. The main curve and transparent regions are the mean and standard deviation across different images, respectively.

	Scene	Armadillo	Dragon	Lucy	Thai Statue	Avg
IOU $\uparrow$	RHINO (DINER)	0.990	0.985	0.966	0.973	0.978
	RHINO (NGP)	0.990	0.985	0.968	0.980	0.981
	Bacon	0.990	0.981	0.969	0.979	0.980
	DINER	0.976	0.978	0.955	0.971	0.970
	Instant NGP	0.990	0.983	0.967	0.980	0.980
Chamfer $\downarrow$	RHINO (DINER)	3.230e-6	1.891e-6	3.011e-6	1.927e-6	2.515e-6
	RHINO (NGP)	3.215e-6	1.853e-6	2.909e-6	1.898e-6	2.469e-6
	Bacon	3.243e-6	1.895e-6	3.052e-6	1.945e-6	2.533e-6
	DINER	2.766e-5	8.758e-6	1.662e-5	1.076e-5	1.595e-5
	Instant NGP	3.228e-6	1.859e-6	2.899e-6	1.904e-6	2.475e-6
Time (min.) $\downarrow$	RHINO (DINER)	62.48	56.15	148.93	344.88	153.11
	RHINO (NGP)	0.60	0.73	0.98	1.73	1.01
	Bacon	82.10	77.60	163.90	334.92	164.63
	DINER	55.27	49.23	132.40	324.47	140.34
	Instant NGP	0.57	0.72	0.98	1.72	1.00

Table 2: Quantitative comparison on 3D shape representation. We color code each cell as best, second best.

orange and the box in the Orange as well as the corn in the Cake in Fig. 6. RHINO rebuilds the analytical connection between the input coordinate and the output attribute, as a result, the noisy artifacts could be significantly alleviated when the RHINO is applied to these hash-based INRs.

Fig. 7 shows the PSNR of various methods for fitting the sampled 1/4 pixels at different epochs. Hash-based methods (DINER and Instant NGP) outperform the function-expansion-based methods (SIREN and PE+MLP). RHINO further improves the accuracy of these hash-based methods while the trend of the curves are also similar with their original versions. Additionally, it is noticed that RHINO (NGP) provides more stable training behavior compared with the original Instant NGP (*e.g.*, the green curve has a smaller fluctuating range than the purple curve). Tab. 1 lists the training time of 3000 epochs. RHINO is slightly slower than the function-expansion-based INRs.

## 5.2 3D Shape Representation

In this section, we demonstrate the representation capabilities of RHINO for representing 3D shapes as SDF, which measures the distance  $s$  between the given spatial point  $\vec{x}$  and the closest surface as a continuous function. The sign of the distance indicates whether the point is inside (negative) or outside (positive) the watertight surface,

$$\text{SDF}(\vec{x}) = s : \vec{x} \in \mathbb{R}^3, s \in \mathbb{R}. \quad (7)$$

To visualize this implicit surface, it can be rendered using raycasting or rasterization techniques on a mesh generated by algorithms such as Marching Cubes (Lorensen and Cline, 1998). This method allows us to convert the representation of the shape into a more tangible and visually interpretable form, enabling visualization and analysis of the 3D surface.

In the experiment, four shapes from the Laboratory (2014) are used for evaluation, namely the Armadillo, Dragon, Lucy, and Thai Statue. In the experiment, 10k points are randomly sampled in each iteration during the training process (the same points are used in all methods), then a 512 cubed grid is extracted for evaluation and visualization. Three baselines are compared, *i.e.*, Bacon (Lindell et al., 2022), DINER (Xie et al., 2023) and Instant NGP (Müller et al., 2022). The performance of the RHINO is verified by applying it to the latter two hash-based methods.

Tab. 2 provides a quantitative comparison of the performance of various methods. RHINO demonstrates significant improvements in both DINER and Instant NGP across almost all four shapes. Furthermore, the increase in computational time for RHINO compared to their original versions is minimal (*e.g.*, 153.11 vs. 140.34 and 1.01 vs. 1.00). It's worth noting that Instant NGP and its RHINO version require considerably less time than other methods. This can be attributed to the rapid convergence of Instant NGP, which achieves convergence in just 2,000 iterations compared to 200,000 for other methods. Additionally, it's noteworthy that the relative increase in time cost (approximately 9% from (153–140)/140) in this context is much smaller than that observed in image fitting (approximately 36% from (15 – 11)/11). This disparity arises because the construction of the loss function contributes more to computational cost in SDF fitting tasks compared to running the network.

Fig. 8 visualizes the difference in reconstructed details. Because the learned function takes the hash-key as an independent variable instead of the coordinate-self, DINER produces undesired artifacts in interpolated areas such as the bulge in the elephant ear and leg in Thai Statue and the squama in Dragon. RHINO (DINER) overcomes this problem and produces more smooth results. Instant NGP alleviates the problem by introducing multi-scale hash grids,

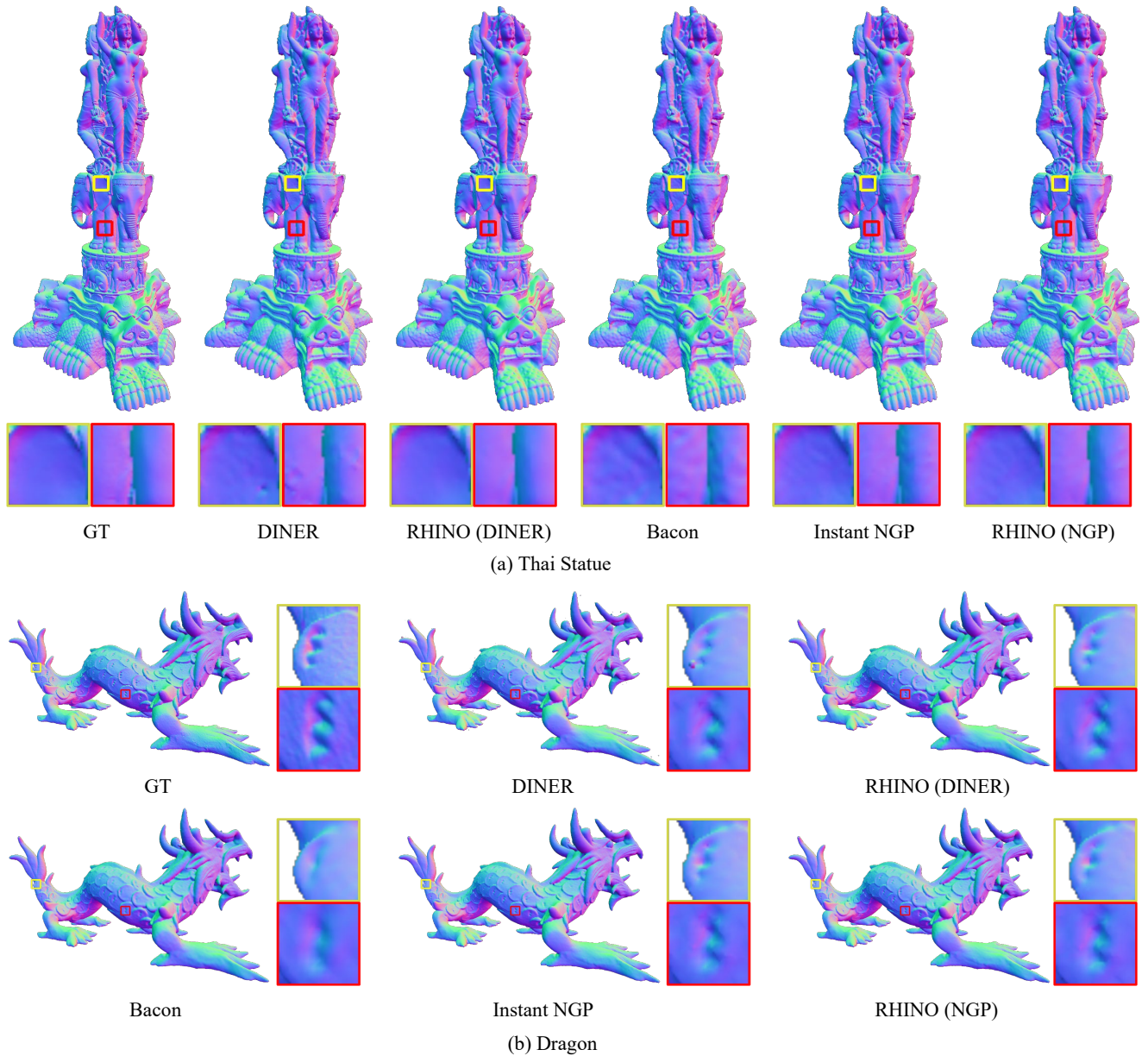


Fig. 8: Shape fitting results. The results indicate that our approach outperforms other methods in representing 3D shapes by effectively capturing smoothness, while other methods exhibit noise artifacts.

however, similar artifacts also appear in the gap between the elephant legs (zoom-in red box in Thai Statue of Fig. 8). RHINO (NGP) also improves Instant NGP with more clear reconstructed legs. Bacon focuses on reconstructing the SDF signal following a scale-by-scale behavior using the sin base function, therefore the unpopular harmonics wave appears in the reconstructed elephant ear and leg which should have smooth surfaces.

In contrast to the task of image fitting, the enhancements achieved by RHINO in SDF representation appear relatively modest. This can be ascribed to the distinct sampling strategies employed. In image fitting, uniform samplings span the

entire domain, whereas in SDF representation, only points proximate to the surface are sampled. Because the points requiring interpolation in SDF representation are closer to the trained points compared to the situation in image fitting, the relative improvement in SDF representation is less pronounced than what is observed in image fitting.

### 5.3 Neural Radiance Fields.

NeRF (Mildenhall et al., 2020) is a highly popular method for novel view synthesis. This technique renders images from

	Scene	Materials	Hotdog	Ship	Mic	Drums	Lego	Chair	Ficus	Avg
PSNR↑	RHINO (DVGO)	30.36	38.69	31.90	36.15	26.61	36.27	37.43	32.71	33.77
	RHINO (NGP)	29.49	38.29	32.05	36.68	26.33	35.86	36.89	33.25	33.61
	NeRF	29.39	36.73	29.17	33.08	25.61	31.54	33.90	28.94	31.04
	Plenoxels	29.18	36.03	29.25	32.95	25.44	31.71	33.74	29.59	30.99
	Instant NGP	29.80	38.24	31.75	36.48	26.24	35.78	36.88	33.03	33.53
	DVGO	30.23	38.48	31.73	35.85	26.50	36.11	37.26	32.37	33.57
	DINER	30.21	37.90	31.25	35.39	26.37	35.13	36.98	32.19	33.18
SSIM↑	RHINO (DVGO)	0.963	0.987	0.917	0.990	0.942	0.986	0.989	0.983	0.970
	RHINO (NGP)	0.953	0.974	0.911	0.988	0.938	0.982	0.985	0.983	0.964
	NeRF	0.957	0.978	0.875	0.978	0.930	0.964	0.975	0.963	0.953
	Plenoxels	0.958	0.977	0.898	0.977	0.932	0.967	0.973	0.969	0.956
	Instant NGP	0.956	0.974	0.912	0.988	0.938	0.981	0.985	0.982	0.964
	DVGO	0.962	0.987	0.915	0.989	0.940	0.986	0.989	0.982	0.969
	DINER	0.964	0.984	0.909	0.988	0.941	0.984	0.989	0.981	0.967
LPIPS↓	RHINO (DVGO)	10.039	0.016	0.079	0.009	0.054	0.011	0.013	0.020	0.030
	RHINO (NGP)	0.064	0.025	0.084	0.012	0.071	0.013	0.016	0.022	0.038
	NeRF	0.044	0.030	0.142	0.028	0.075	0.038	0.033	0.043	0.054
	Plenoxels	0.044	0.033	0.112	0.029	0.069	0.037	0.036	0.038	0.050
	Instant NGP	0.060	0.024	0.081	0.014	0.072	0.014	0.016	0.024	0.038
	DVGO	0.040	0.017	0.080	0.009	0.057	0.012	0.013	0.022	0.031
	DINER	0.037	0.025	0.086	0.011	0.054	0.014	0.013	0.026	0.033
Time↓	RHINO (DVGO)	407.32	366.77	483.44	234.34	287.59	305.44	284.31	300.68	333.74
	RHINO (NGP)	376.37	387.26	486.21	355.80	358.14	381.07	368.52	374.29	385.96
	NeRF	10841.14	10841.13	11144.72	10806.78	10822.55	10847.77	10883.87	10905.11	10886.63
	Plenoxels	297.88	325.47	360.98	277.08	289.42	302.71	305.58	280.80	304.99
	Instant NGP	335.16	349.03	400.50	326.25	352.41	335.63	324.44	318.67	342.76
	DVGO	223.75	269.85	239.80	155.85	171.59	181.96	177.03	179.26	199.89
	DINER	448.54	467.99	492.14	272.30	337.73	467.59	432.39	422.68	417.67

Table 3: Quantitative comparison on static novel view synthesis. We color code each cell as **best**, **second best**, and **third best**.

novel viewpoints using multiple input images with known in/extrinsic matrixes. NeRF achieves this by mapping 3D spatial coordinates  $\vec{x}$  and viewing directions  $\vec{d}$  to corresponding density  $\sigma$  and color emission  $c$ . To render the color of a pixel  $\hat{C}(r)$ , we firstly calculate the ray function of the  $r$  using the in/extrinsic matrixes. Next, we sample  $N$  points along the ray within a predefined depth range. Then, the coordinates and the directions of these  $N$  samples are used to query their corresponding density and color (as performed by the MLP in NeRF). Finally, the color  $\hat{C}(r)$  is obtained by applying the volume rendering techniques (Max, 1995) to the queried attributes,

$$\begin{aligned} \hat{C}(r) &= \sum_{i=1}^N T_i (1 - \exp(-\sigma_i \delta_i)) c_i \\ T_i &= \exp \left( - \sum_{j=1}^{i-1} \sigma_j \delta_j \right), \end{aligned} \quad (8)$$

where  $T_i$  represents the proportion of light transmitted through ray  $r$  to sample  $i$  relative to the contribution of preceding samples. The term  $1 - \exp(-\sigma_i \delta_i)$  denotes the amount of light contributed by sample  $i$ , where  $\sigma_i$  and  $c_i$  represent the opac-

ity and color of sample  $i$ , respectively. The term  $\delta_i$  represents the distance between the neighboring samples.

Because the rays emitted from the input images could not cover the entire space, it is unavoidable to interpolate unsampled points when the images of novel views are rendered. As a result, it is important to design an INR with good regularization. In our experiment, five baselines are compared, namely, the NeRF, the Plenoxels (Fridovich-Keil et al., 2022), the DINER (Zhu et al., 2023a), the DVGO (Sun et al., 2022) and the Instant NGP (Müller et al., 2022). Among these methods, although the DINER, the DVGO and the Instant NGP all adopts the hash-based strategy, the latter two are selected for verifying the improvement of the RHINO since the DINER (Zhu et al., 2023a) outputs the spherical harmonics coefficients (Yu et al., 2021; Fridovich-Keil et al., 2022) instead of the attributes ( $\sigma, c$ ) directly.

Tab. 3 and Fig. 9 offer both quantitative and qualitative comparisons of RHINO against various methods using the down-scaled Blender dataset (Mildenhall et al., 2020), which has a resolution of  $400 \times 400$ . In Tab. 3, the original DVGO and Instant NGP initially deliver competitive results among the five methods under consideration. However, RHINO, our

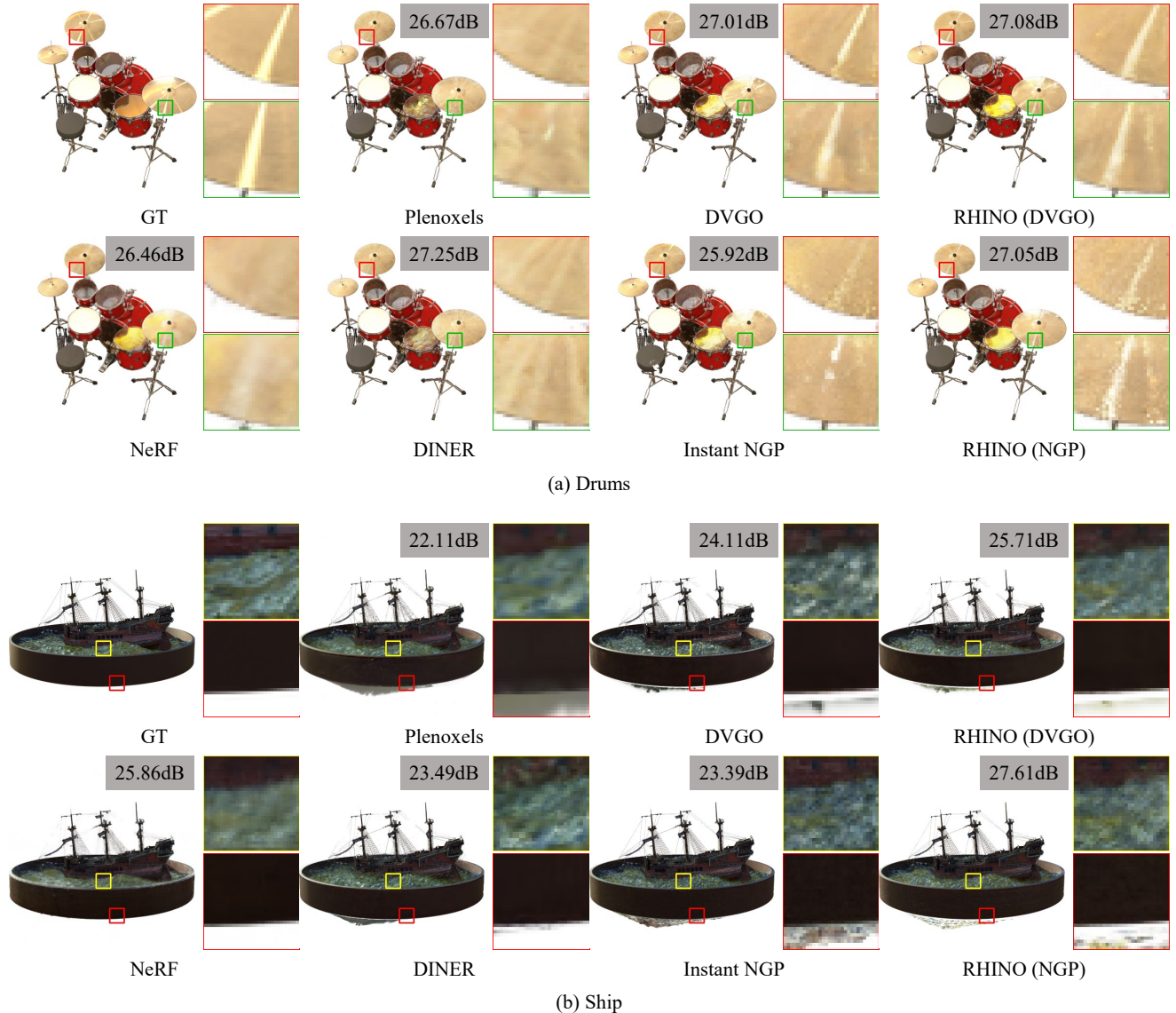


Fig. 9: Qualitative comparisons of RHINO with the SOTAs on the task of the static novel view synthesis. In 'Drums', RHINO interpolate more reasonable textures while other methods yield smoother reconstructions. In 'Ship', RHINO suppresses the artifacts appeared in the DVGO and the Instant NGP, producing more smooth results in the red box.

proposed approach, further enhances their performance and ultimately achieves the best results.

Fig. 9 demonstrates these advantages well. In the example of 'Drums', the image enclosed in the red and yellow boxes demonstrate visually appealing smooth textures. Due to the broken gradients flow as mentioned above, previous hash-based methods all produce undesired artifacts in these areas which are not sampled in the training set. RHINO rebuilds the gradients connection between the input coordinate and the output attributes, thus more reasonable textures are interpolated here. These advantages are similarly evident in the 'Ship' example, where both the waves (yellow box) and the hull bottom (red box) are sparsely sampled. RHINO effec-

tively suppresses the artifacts observed in DVGO and Instant NGP, resulting in smoother outcomes in these under-sampled regions.

#### 5.4 Dynamic Novel View Synthesis

Building upon the success of NeRF for static scenes, the application of NeRF and its variants to dynamic novel view synthesis has garnered increasing attention in recent times. However, owing to the substantial volume of input data derived from multiple videos captured from different views, function-expansion-based INRs often necessitate large networks to capture intricate spatial and temporal details. This

	Scene	Cook-Spinach	Flame-Steak	Sear-Steak	Cut-Roasted-Beef	Avg
PSNR↑	Kplanes	31.16	31.85	32.10	32.99	32.03
	MixVoxels	32.23	31.96	31.60	32.94	32.18
	DINER	31.93	32.76	33.07	32.01	32.44
	RHINO	32.34	33.51	33.60	32.53	33.00
SSIM↑	Kplanes	0.932	0.953	0.952	0.940	0.944
	MixVoxels	0.940	0.947	0.949	0.943	0.945
	DINER	0.936	0.944	0.948	0.935	0.941
	RHINO	0.941	0.950	0.953	0.942	0.947
LPIPS↓	Kplanes	0.192	0.175	0.178	0.190	0.184
	MixVoxels	0.140	0.135	0.134	0.141	0.138
	DINER	0.173	0.174	0.165	0.181	0.173
	RHINO	0.164	0.161	0.155	0.170	0.163
Time↓	Kplanes	52.07	48.7	47.37	48.78	49.23
	MixVoxels	47.12	44.50	45.75	48.42	46.45
	DINER	40.76	41.52	38.25	43.79	41.08
	RHINO	46.78	45.43	46.36	45.35	45.98

Table 4: Quantitative comparison on dynamic view synthesis. We color code each cell as best (red), second best (orange).

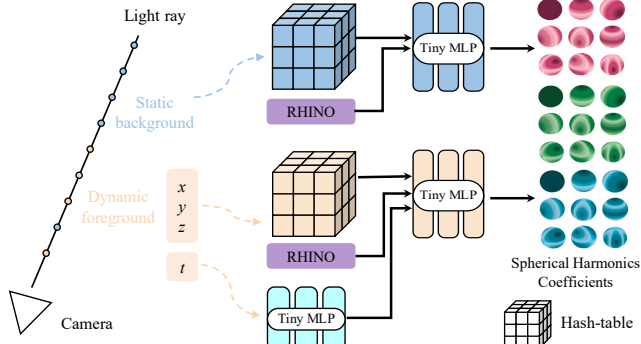


Fig. 10: The pipeline of the dynamic NeRF using the RHINO.

results in prohibitive time costs for training dynamic NeRF models, such as the 1300 GPU hours reported in Li et al. (2022). As a solution, hash-based INRs have gained widespread adoption in dynamic novel view synthesis tasks, as demonstrated by approaches like Kplanes (Fridovich-Keil et al., 2023), Hexplanes (Cao and Johnson, 2023), and MixVoxels (Wang et al., 2022). In our implementation, we leverage RHINO with the DINER backbone (Zhu et al., 2023a) for dynamic novel view synthesis, as depicted in Fig. 10. The 3D environment is initially partitioned into static background and dynamic foreground regions, following the methodology outlined in MixVoxels Wang et al. (2022). Subsequently, the spherical harmonic coefficients of these background and foreground points are modeled using two independent hash-based INRs. It is worth noting that instead of employing a hash-table, the time parameter  $t$  is fed into an additional MLP. Finally, the view-dependent color of the 3D point is computed by querying the spherical harmonic functions based on the desired viewing direction (Yu et al., 2021). The size of the

hash-table is set as  $256^3$  with width 28 in our implementation.

We conduct our performance evaluation of RHINO using the dataset introduced by Li et al. (2022). This dataset comprises videos captured at a high resolution of  $2028 \times 2704$  pixels, with a frame rate of 30 FPS, and encompasses 21 distinct views. In our experiments, 10 seconds (corresponding to 300 frames of all images) from the 20 views are used for training, while the frames from the remaining view were reserved for testing. To maintain consistency, we scaled the image resolution to  $507 \times 676$  pixels for all methods. For benchmarking purposes, we selected two SOTA methods, specifically Kplanes (Fridovich-Keil et al., 2023) and MixVoxels (Wang et al., 2022), for comparison. We adhered to the default configurations outlined in their respective original implementations, following their recommended settings.

Tab. 4 offers a quantitative comparison of the results. It's worth noting that RHINO outperforms the DINER backbone in all metrics, except for the additional time costs. When compared with SOTA methods, RHINO achieves the highest PSNR and SSIM scores and ranks second in terms of LPIPS values. Furthermore, RHINO demonstrates competitive training times, particularly when compared to Kplanes (Fridovich-Keil et al., 2023), which is a popular approach for accelerating the processing of high-dimensional signals (Shao et al., 2023; Singer et al., 2023; Shue et al., 2023).

Fig. 11 offers a visual comparison of the results. Notably, in DINER, artifacts become apparent due to the broken gradient flow. For instance, observe the bent or missing handle of the spatula in Fig. 11, particularly in the zoomed-in yellow boxes found in both the top and bottom subfigures. RHINO effectively rebuilds the gradient flow, resulting in more coherent reconstructions in these problematic regions. It's noteworthy that some of the artifacts observed in DINER

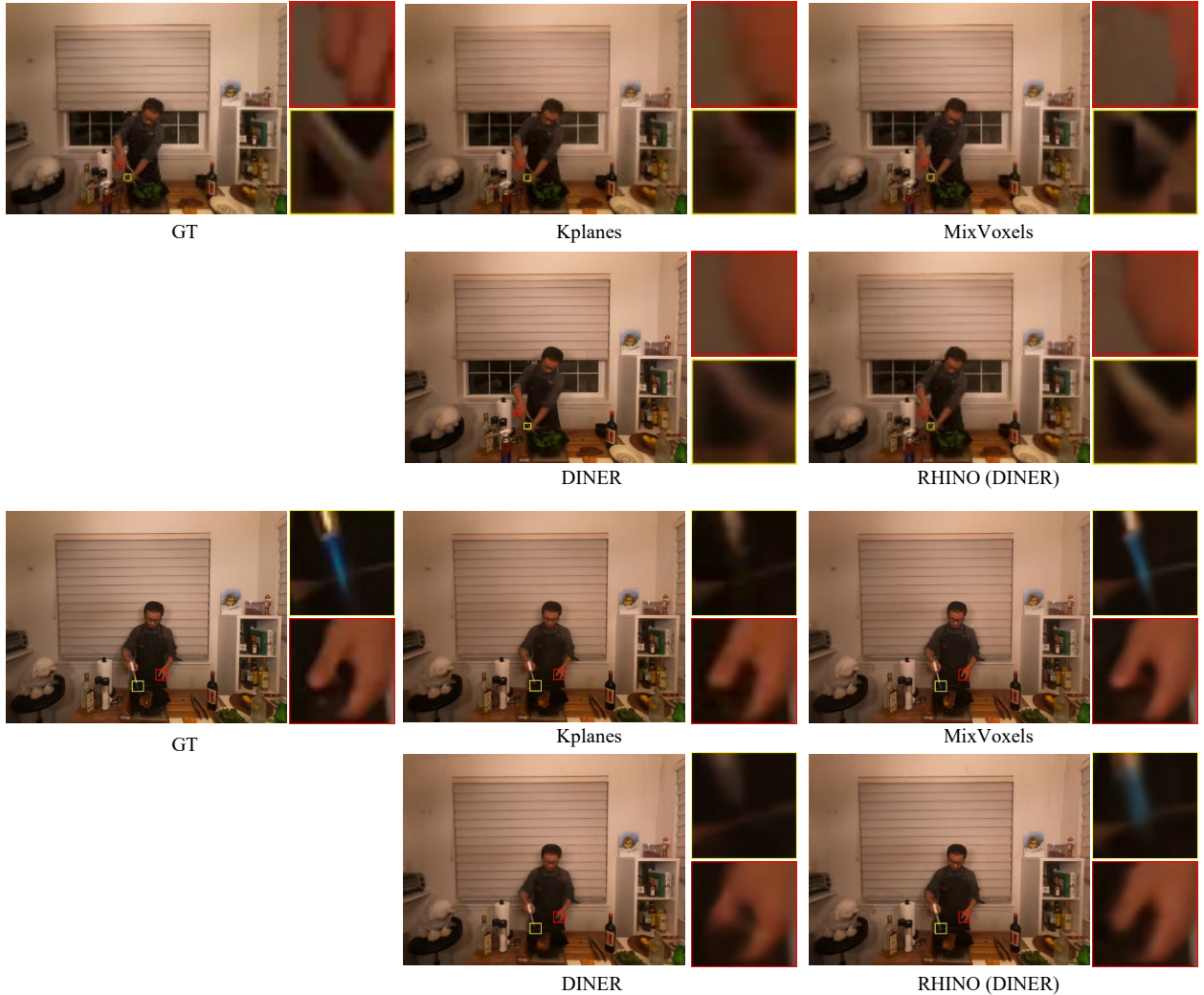


Fig. 11: Qualitative comparison on dynamic novel view synthesis.

also persist or are exacerbated in Kplanes. This phenomenon may be attributed to the fact that in Kplanes, the input coordinates are also hash-indexed when optimizing various planes. While MixVoxels are capable of yielding clearer results, as evident in the example of the blue spatula handle in the bottom subfigure, they are occasionally prone to block artifacts. Conversely, RHINO offers more consistent reconstructions, albeit at times with the trade-off of textures appearing overly smoothed.

## 6 Conclusion

In this work, we have proposed the RHINO which is a universal method for regularizing current hash-based INRs and thus enhancing the performance of interpolations. We have pointed out that the noisy interpolations suffered in SOTA hash-based INRs are caused by the broken gradients flow between the coordinates input and the indexed hash-keys for

feeding into the network. The proposed RHINO rebuilds the gradients flow by introducing a connection from the coordinate to the network directly, for which the gradients flow could be propagated from the network output to the coordinate unobstructively. For this reason, the noisy interpolation artifacts of different hash-based INRs could be significantly alleviated. Extensive experiments have verified the high accuracy and regularization performance of the proposed RHINO for various fitting and inverse problem optimization tasks.

## Acknowledgements

We thank the Prof. David B. Lindell for the help of evaluating the results of the SDF.

## Data Availability Statements

The datasets used for the image representation, 3D shape representation, as well as the 5D static/6D dynamic NeRF come from the public datasets ([Asuni and Giachetti, 2014; Laboratory, 2014; Mildenhall et al., 2020; Li et al., 2022](#)). All codes and models will be publicly available to the research community to facilitate reproducible research once the paper is accepted. The datasets generated during and/or analysed during the current study are available from the corresponding author on reasonable request.

## References

- Abdal R, Qin Y, Wonka P (2019) Image2stylegan: How to embed images into the stylegan latent space? In: *Proceedings of the IEEE/CVF international conference on computer vision*, pp 4432–4441
- Abou-Chakra J, Dayoub F, Sünderhauf N (2022) Particlenerf: Particle based encoding for online neural radiance fields in dynamic scenes. *arXiv preprint arXiv:221104041*
- Asuni N, Giachetti A (2014) Testimages: a large-scale archive for testing visual devices and basic image processing algorithms. In: *STAG*, pp 63–70
- Bao C, Zhang Y, Yang B, Fan T, Yang Z, Bao H, Zhang G, Cui Z (2023) Sine: Semantic-driven image-based nerf editing with prior-guided editing field. In: *Proceedings of the IEEE/CVF Conference on Computer Vision and Pattern Recognition*, pp 20919–20929
- Barron JT, Mildenhall B, Tancik M, Hedman P, Martin-Brualla R, Srinivasan PP (2021) Mip-nerf: A multiscale representation for anti-aliasing neural radiance fields. In: *Proceedings of the IEEE/CVF International Conference on Computer Vision*, pp 5855–5864
- Cao A, Johnson J (2023) Hexplane: A fast representation for dynamic scenes. In: *Proceedings of the IEEE/CVF Conference on Computer Vision and Pattern Recognition*, pp 130–141
- Chabra R, Lenssen JE, Ilg E, Schmidt T, Straub J, Lovegrove S, Newcombe R (2020) Deep local shapes: Learning local sdf priors for detailed 3d reconstruction. In: *European Conference on Computer Vision*, Springer, pp 608–625
- Chan ER, Lin CZ, Chan MA, Nagano K, Pan B, De Mello S, Gallo O, Guibas LJ, Tremblay J, Khamis S, et al. (2022) Efficient geometry-aware 3d generative adversarial networks. In: *Proceedings of the IEEE/CVF Conference on Computer Vision and Pattern Recognition*, pp 16123–16133
- Chen A, Xu Z, Zhao F, Zhang X, Xiang F, Yu J, Su H (2021) MVS-NeRF: Fast generalizable radiance field reconstruction from multi-view stereo. In: *Proceedings of the IEEE/CVF International Conference on Computer Vision*, pp 14124–14133
- Chen A, Xu Z, Geiger A, Yu J, Su H (2022) Tensorf: Tensorial radiance fields. In: *European Conference on Computer Vision*, Springer, pp 333–350
- Chen Y, Lu L, Karniadakis GE, Dal Negro L (2020) Physics-informed neural networks for inverse problems in nano-optics and metamaterials. *Optics express* 28(8):11618–11633
- Dupont E, Goliński A, Alizadeh M, Teh YW, Doucet A (2021) Coin: Compression with implicit neural representations. *arXiv preprint arXiv:210303123*
- Fang J, Yi T, Wang X, Xie L, Zhang X, Liu W, Nießner M, Tian Q (2022) Fast dynamic radiance fields with time-aware neural voxels. In: *SIGGRAPH Asia 2022 Conference Papers*, pp 1–9
- Fathony R, Sahu AK, Willmott D, Kolter JZ (2020) Multiplicative filter networks. In: *International Conference on Learning Representations*
- Fridovich-Keil S, Yu A, Tancik M, Chen Q, Recht B, Kanazawa A (2022) Plenoxels: Radiance fields without neural networks. In: *Proceedings of the IEEE/CVF Conference on Computer Vision and Pattern Recognition*, pp 5501–5510
- Fridovich-Keil S, Meanti G, Warburg FR, Recht B, Kanazawa A (2023) K-planes: Explicit radiance fields in space, time, and appearance. In: *Proceedings of the IEEE/CVF Conference on Computer Vision and Pattern Recognition*, pp 12479–12488
- Gao R, Si Z, Chang YY, Clarke S, Bohg J, Fei-Fei L, Yuan W, Wu J (2022) Objectfolder 2.0: A multisensory object dataset for sim2real transfer. In: *Proceedings of the IEEE/CVF Conference on Computer Vision and Pattern Recognition*, pp 10598–10608
- Genova K, Cole F, Sud A, Sarna A, Funkhouser T (2020) Local deep implicit functions for 3d shape. In: *Proceedings of the IEEE/CVF international conference on computer vision*, pp 4857–4866
- Goodfellow I, Pouget-Abadie J, Mirza M, Xu B, Warde-Farley D, Ozair S, Courville A, Bengio Y (2014) Generative adversarial nets. *Advances in neural information processing systems* 27
- Heiss J, Teichmann J, Wutte H (2019) How implicit regularization of relu neural networks characterizes the learned function—part i: the 1-d case of two layers with random first layer. *arXiv preprint arXiv:191102903*
- Ho J, Jain A, Abbeel P (2020) Denoising diffusion probabilistic models. *Advances in neural information processing systems* 33:6840–6851
- Hu Z, Nie F, Wang R, Li X (2021) Low rank regularization: A review. *Neural Networks* 136:218–232
- Huang J, Thies J, Dai A, Kundu A, Jiang C, Guibas LJ, Nießner M, Funkhouser T, et al. (2020) Adversarial texture optimization from rgb-d scans. In: *Proceedings of the IEEE/CVF Conference on Computer Vision and Pattern Recognition*, pp 1559–1568
- Huang X, Zhang Q, Feng Y, Li H, Wang X, Wang Q (2022) Hdr-nerf: High dynamic range neural radiance fields. In: *Proceedings of the IEEE/CVF Conference on Computer Vision and Pattern Recognition*, pp 18398–18408
- Huang X, Zhang Q, Feng Y, Li H, Wang Q (2023a) Inverting the imaging process by learning an implicit camera model. In: *Proceedings of the IEEE/CVF Conference on Computer Vision and Pattern Recognition*, pp 21456–21465
- Huang X, Zhang Q, Feng Y, Li X, Wang X, Wang Q (2023b) Local implicit ray function for generalizable radiance field representation. In: *Proceedings of the IEEE/CVF Conference on Computer Vision and Pattern Recognition*, pp 97–107
- Jacot A, Gabriel F, Hongler C (2018) Neural tangent kernel: Convergence and generalization in neural networks. *Advances in neural information processing systems* 31
- Jiang C, Sud A, Makadia A, Huang J, Nießner M, Funkhouser T, et al. (2020) Local implicit grid representations for 3d scenes. In: *Proceedings of the IEEE/CVF Conference on Computer Vision and Pattern Recognition*, pp 6001–6010
- Johari MM, Lepoittevin Y, Fleuret F (2022) GeoNeRF: Generalizing nerf with geometry priors. In: *Proceedings of the IEEE/CVF Conference on Computer Vision and Pattern Recognition*, pp 18365–18375
- Kang N, Lee B, Hong Y, Yun SB, Park E (2022) Pixel: Physics-informed cell representations for fast and accurate pde solvers. *arXiv preprint arXiv:220712800*
- Karniadakis GE, Kevrekidis IG, Lu L, Perdikaris P, Wang S, Yang L (2021) Physics-informed machine learning. *Nature Reviews Physics* 3(6):422–440
- Kasten Y, Ofri D, Wang O, Dekel T (2021) Layered neural atlases for consistent video editing. *ACM Transactions on Graphics (TOG)* 40(6):1–12
- Kubo M, Banno R, Manabe H, Minoji M (2019) Implicit regularization in over-parameterized neural networks. *arXiv preprint arXiv:190301997*
- Laboratory SCG (2014) The stanford 3d scanning repository. [Http://graphics.stanford.edu/data/3Dscanrep/](http://graphics.stanford.edu/data/3Dscanrep/)

- Li T, Slavcheva M, Zollhoefer M, Green S, Lassner C, Kim C, Schmidt T, Lovegrove S, Goesele M, Newcombe R, et al. (2022) Neural 3d video synthesis from multi-view video. In: *Proceedings of the IEEE/CVF Conference on Computer Vision and Pattern Recognition*, pp 5521–5531
- Li Z, Wang H, Meng D (2023a) Regularize implicit neural representation by itself. In: *Proceedings of the IEEE/CVF Conference on Computer Vision and Pattern Recognition*, pp 10280–10288
- Li Z, Wang Q, Cole F, Tucker R, Snavely N (2023b) Dynibar: Neural dynamic image-based rendering. In: *Proceedings of the IEEE/CVF Conference on Computer Vision and Pattern Recognition*, pp 4273–4284
- Lin CH, Gao J, Tang L, Takikawa T, Zeng X, Huang X, Kreis K, Fidler S, Liu MY, Lin TY (2023) Magic3d: High-resolution text-to-3d content creation. In: *Proceedings of the IEEE/CVF Conference on Computer Vision and Pattern Recognition*, pp 300–309
- Lindell DB, Van Veen D, Park JJ, Wetzstein G (2021) Bacon: Band-limited coordinate networks for multiscale scene representation. In: *Proceedings of the IEEE/CVF conference on computer vision and pattern recognition*
- Lindell DB, Van Veen D, Park JJ, Wetzstein G (2022) Bacon: Band-limited coordinate networks for multiscale scene representation. In: *Proceedings of the IEEE/CVF conference on computer vision and pattern recognition*, pp 16252–16262
- Liu L, Gu J, Zaw Lin K, Chua TS, Theobalt C (2020) Neural sparse voxel fields. *Advances in Neural Information Processing Systems* 33:15651–15663
- Liu R, Sun Y, Zhu J, Tian L, Kamilov US (2022) Recovery of continuous 3d refractive index maps from discrete intensity-only measurements using neural fields. *Nature Machine Intelligence* 4(9):781–791
- Lombardi S, Simon T, Saragih J, Schwartz G, Lehrmann A, Sheikh Y (2019) Neural volumes: learning dynamic renderable volumes from images. *ACM Transactions on Graphics (TOG)* 38(4):1–14
- Lorensen WE, Cline HE (1998) Marching cubes: A high resolution 3d surface construction algorithm. In: Seminal graphics: pioneering efforts that shaped the field, pp 347–353
- Maennel H, Bousquet O, Gelly S (2018) Gradient descent quantizes relu network features. *arXiv preprint arXiv:180308367*
- Martin-Brualla R, Radwan N, Sajjadi MS, Barron JT, Dosovitskiy A, Duckworth D (2021) Nerf in the wild: Neural radiance fields for unconstrained photo collections. In: *Proceedings of the IEEE/CVF Conference on Computer Vision and Pattern Recognition*, pp 7210–7219
- Max N (1995) Optical models for direct volume rendering. *IEEE Transactions on Visualization and Computer Graphics* 1(2):99–108
- Mescheder L, Oechsle M, Niemeyer M, Nowozin S, Geiger A (2019) Occupancy networks: Learning 3d reconstruction in function space. In: *Proceedings of the IEEE/CVF Conference on Computer Vision and Pattern Recognition*, pp 4460–4470
- Mildenhall B, Srinivasan PP, Tancik M, Barron JT, Ramamoorthi R, Ng R (2020) Nerf: Representing scenes as neural radiance fields for view synthesis. In: *European conference on computer vision*, Springer, pp 405–421
- Müller T (2021) Tiny cuda neural network framework. <https://github.com/nvlabz/tiny-cuda-nn>
- Müller T, Evans A, Schied C, Keller A (2022) Instant neural graphics primitives with a multiresolution hash encoding. *ACM Transactions on Graphics (ToG)* 41(4):1–15
- Nichol AQ, Dhariwal P (2021) Improved denoising diffusion probabilistic models. In: *International Conference on Machine Learning*, PMLR, pp 8162–8171
- Niemeyer M, Mescheder L, Oechsle M, Geiger A (2019) Occupancy flow: 4d reconstruction by learning particle dynamics. In: *Proceedings of the IEEE/CVF international conference on computer vision*, pp 5379–5389
- Or-El R, Luo X, Shan M, Shechtman E, Park JJ, Kemelmacher-Shlizerman I (2022) Stylesdf: High-resolution 3d-consistent image and geometry generation. In: *Proceedings of the IEEE/CVF Conference on Computer Vision and Pattern Recognition*, pp 13503–13513
- Peng S, Niemeyer M, Mescheder L, Pollefeys M, Geiger A (2020) Convolutional occupancy networks. In: *European Conference on Computer Vision*, Springer, pp 523–540
- Poole B, Jain A, Barron JT, Mildenhall B (2022) Dreamfusion: Text-to-3d using 2d diffusion. In: *International Conference on Learning Representations*
- Pumarola A, Popov S, Moreno-Noguer F, Ferrari V (2020) C-flow: Conditional generative flow models for images and 3d point clouds. In: *Proceedings of the IEEE/CVF Conference on Computer Vision and Pattern Recognition*, pp 7949–7958
- Rahaman N, Baratin A, Arpit D, Draxler F, Lin M, Hamprecht F, Bengio Y, Courville A (2019) On the spectral bias of neural networks. In: *International Conference on Machine Learning*, PMLR, pp 5301–5310
- Raissi M, Perdikaris P, Karniadakis GE (2019) Physics-informed neural networks: A deep learning framework for solving forward and inverse problems involving nonlinear partial differential equations. *Journal of Computational Physics* 378:686–707
- Raissi M, Yazdani A, Karniadakis GE (2020) Hidden fluid mechanics: Learning velocity and pressure fields from flow visualizations. *Science* 367(6481):1026–1030
- Ramasinghe S, Lucey S (2022) Beyond periodicity: towards a unifying framework for activations in coordinate-mlps. In: *Computer Vision–ECCV 2022: 17th European Conference, Tel Aviv, Israel, October 23–27, 2022, Proceedings, Part XXXIII*, Springer, pp 142–158
- Ramasinghe S, MacDonald LE, Lucey S (2022) On the frequency-bias of coordinate-mlps. *Advances in Neural Information Processing Systems* 35:796–809
- Rückert D, Franke L, Stamminger M (2022) Adop: Approximate differentiable one-pixel point rendering. *ACM Transactions on Graphics (TOG)* 41(4):1–14
- Rudin LI, Osher S, Fatemi E (1992) Nonlinear total variation based noise removal algorithms. *Physica D: nonlinear phenomena* 60(1–4):259–268
- Saharia C, Chan W, Saxena S, Li L, Whang J, Denton EL, Ghasemipour K, Gontijo Lopes R, Karagol Ayan B, Salimans T, et al. (2022) Photorealistic text-to-image diffusion models with deep language understanding. *Advances in Neural Information Processing Systems* 35:36479–36494
- Saragadam V, LeJeune D, Tan J, Balakrishnan G, Veeraghavan A, Baraniuk RG (2023) Wire: Wavelet implicit neural representations. In: *Proceedings of the IEEE/CVF Conference on Computer Vision and Pattern Recognition (CVPR)*, pp 18507–18516
- Shao R, Zheng Z, Tu H, Liu B, Zhang H, Liu Y (2023) Tensor4d: Efficient neural 4d decomposition for high-fidelity dynamic reconstruction and rendering. In: *Proceedings of the IEEE/CVF Conference on Computer Vision and Pattern Recognition*, pp 16632–16642
- Shue JR, Chan ER, Po R, Ankner Z, Wu J, Wetzstein G (2023) 3d neural field generation using triplane diffusion. In: *Proceedings of the IEEE/CVF Conference on Computer Vision and Pattern Recognition*, pp 20875–20886
- Singer U, Sheynin S, Polyak A, Ashual O, Makarov I, Kokkinos F, Goyal N, Vedaldi A, Parikh D, Johnson J, et al. (2023) Text-to-4d dynamic scene generation. *arXiv preprint arXiv:230111280*
- Sitzmann V, Thies J, Heide F, Nießner M, Wetzstein G, Zollhofer M (2019) Deepvoxels: Learning persistent 3d feature embeddings. In: *Proceedings of the IEEE/CVF Conference on Computer Vision and Pattern Recognition*, pp 2437–2446
- Sitzmann V, Martel J, Bergman A, Lindell D, Wetzstein G (2020) Implicit neural representations with periodic activation functions. *Advances in Neural Information Processing Systems* 33:7462–7473

- Srivastava N, Hinton G, Krizhevsky A, Sutskever I, Salakhutdinov R (2014) Dropout: a simple way to prevent neural networks from overfitting. *The journal of machine learning research* 15(1):1929–1958
- Strümpler Y, Postels J, Yang R, Gool LV, Tombari F (2022) Implicit neural representations for image compression. In: *European Conference on Computer Vision*, Springer, pp 74–91
- Sun C, Sun M, Chen HT (2022) Direct voxel grid optimization: Superfast convergence for radiance fields reconstruction. In: *Proceedings of the IEEE/CVF Conference on Computer Vision and Pattern Recognition*, pp 5459–5469
- Takikawa T, Litalien J, Yin K, Kreis K, Loop C, Nowrouzezahrai D, Jacobson A, McGuire M, Fidler S (2021) Neural geometric level of detail: Real-time rendering with implicit 3d shapes. In: *Proceedings of the IEEE/CVF Conference on Computer Vision and Pattern Recognition*, pp 11358–11367
- Tancik M, Srinivasan P, Mildenhall B, Fridovich-Keil S, Raghavan N, Singhal U, Ramamoorthi R, Barron J, Ng R (2020) Fourier features let networks learn high frequency functions in low dimensional domains. *Advances in Neural Information Processing Systems* 33:7537–7547
- Tang J (2022) Torch-npg: a pytorch implementation of instant-npg. [Https://github.com/ashawkey/torch-npg](https://github.com/ashawkey/torch-npg)
- Tewari A, Thies J, Mildenhall B, Srinivasan P, Tretschk E, Yifan W, Lassner C, Sitzmann V, Martin-Brualla R, Lombardi S, et al. (2022) Advances in neural rendering. In: *Computer Graphics Forum*, Wiley Online Library, vol 41, pp 703–735
- Thies J, Zollhöfer M, Nießner M (2019) Deferred neural rendering: Image synthesis using neural textures. *ACM Transactions on Graphics (TOG)* 38(4):1–12
- Wang F, Tan S, Li X, Tian Z, Liu H (2022) Mixed neural voxels for fast multi-view video synthesis. *arXiv preprint arXiv:221200190*
- Wang N, Zhang Y, Li Z, Fu Y, Liu W, Jiang YG (2018) Pixel2mesh: Generating 3d mesh models from single rgb images. In: *Proceedings of the European conference on computer vision (ECCV)*, pp 52–67
- Wang P, Liu L, Liu Y, Theobalt C, Komura T, Wang W (2021a) Neus: Learning neural implicit surfaces by volume rendering for multi-view reconstruction. *Advances in Neural Information Processing Systems* 34:27171–27183
- Wang PS, Liu Y, Guo YX, Sun CY, Tong X (2017) O-CNN: Octree-based convolutional neural networks for 3D shape analysis. *ACM Transactions on Graphics (TOG)* 36(4):1–11
- Wang Q, Wang Z, Genova K, Srinivasan PP, Zhou H, Barron JT, Martin-Brualla R, Snavely N, Funkhouser T (2021b) IBRNet: Learning multi-view image-based rendering. In: *Proceedings of the IEEE/CVF Conference on Computer Vision and Pattern Recognition*, pp 4690–4699
- Wu M, Wang Y, Hu Q, Yu J (2020) Multi-view neural human rendering. In: *Proceedings of the IEEE/CVF Conference on Computer Vision and Pattern Recognition*, pp 1682–1691
- Xie S, Zhu H, Liu Z, Zhang Q, Zhou Y, Cao X, Ma Z (2023) DINER: Disorder-invariant implicit neural representation. In: *Proceedings of the IEEE/CVF Conference on Computer Vision and Pattern Recognition*, pp 1–10
- Yang G, Benaim S, Jampani V, Genova K, Barron JT, Funkhouser T, Hariharan B, Belongie S (2022) Polynomial neural fields for subband decomposition and manipulation. In: *Advances in Neural Information Processing Systems*, vol 35, pp 1–15
- Yariv L, Gu J, Kasten Y, Lipman Y (2021) Volume rendering of neural implicit surfaces. *Advances in Neural Information Processing Systems* 34:4805–4815
- Yu A, Li R, Tancik M, Li H, Ng R, Kanazawa A (2021) Plenoctrees for real-time rendering of neural radiance fields. In: *Proceedings of the IEEE/CVF International Conference on Computer Vision*, pp 5752–5761
- Yu Z, Peng S, Niemeyer M, Sattler T, Geiger A (2022) Monosdf: Exploring monocular geometric cues for neural implicit surface reconstruction. *Advances in neural information processing systems* 35:25018–25032
- Yuan YJ, Sun YT, Lai YK, Ma Y, Jia R, Gao L (2022) Nerf-editing: geometry editing of neural radiance fields. In: *Proceedings of the IEEE/CVF Conference on Computer Vision and Pattern Recognition*, pp 18353–18364
- Yüce G, Ortiz-Jiménez G, Besbinar B, Frossard P (2022) A structured dictionary perspective on implicit neural representations. In: *Proceedings of the IEEE/CVF Conference on Computer Vision and Pattern Recognition*, pp 19228–19238
- Zhu H, Liu Z, Zhou Y, Ma Z, Cao X (2022) DNF: Diffractive neural field for lensless microscopic imaging. *Optics Express* 30(11):18168–18178
- Zhu H, Xie S, Liu Z, Liu F, Zhang Q, Zhou Y, Lin Y, Ma Z, Cao X (2023a) Disorder-invariant implicit neural representation. *arXiv preprint arXiv:230400837*
- Zhu J, Zhu H, Zhang Q, Zhu F, Ma Z, Cao X (2023b) Pyramid nerf: Frequency guided fast radiance field optimization. *International Journal of Computer Vision* pp 1–16